First-principles investigation of anisotropic magnetic exchange interactions in altermagnetic rutile fluorides

Surasree Sadhukhan [*] and I. I. Mazin

Department of Physics and Astronomy, George Mason University, Fairfax, Virginia 22030, USA
and Quantum Science and Engineering Center, George Mason University, Fairfax, Virginia 22030, USA

(Received 14 October 2025; revised 4 January 2026; accepted 23 January 2026; published 9 February 2026)

A microscopic understanding of magnetic exchange parameters beyond the conventional Heisenberg and Dzyaloshinskii-Moriya interaction (DMI) is crucial for 3*d* difluorides, particularly for NiF_2, where spins are tilting about 0.43° along the *z* axis, which cannot be explained by DMI. It was proposed by Moriya Phys. Rev. **117**, 635 (1960) that this canting is related to single-site anisotropy, but the anisotropic contribution to magnetic exchange remains insufficiently addressed. It is unclear what role anisotropic exchange plays in comparison with single-site anisotropy, which can also induce a spin canting. Motivated by Moriya's work, we have calculated from first principles the full anisotropic exchange matrix for 3*d* rutile difluorides and performed a systematic comparison of MnF_2, FeF_2, CoF_2, and NiF_2. Our approach integrates symmetry-based spin-Hamiltonian construction and first-principles calculations, enabling the determination of the minimal form of the magnetic exchange matrix in the presence of spin-orbit coupling.

DOI: 10.1103/h1ld-4gxc

I. INTRODUCTION

The first proposed altermagnetic was a metallic rutile, ruthenium dioxide (RuO_2). However, subsequent experimental investigations using muon spin-rotation (μSR) techniques, neutron scattering, and other techniques have revealed that RuO_2 is, in fact, nonmagnetic [1–11]. Nevertheless, the rutile crystal structure can host a *d*-wave alternating magnetic order, making it a promising altermagnetic candidate. The 3*d*-metal-based difluorides also adopt the rutile crystal structure and exhibit similar signatures of altermagnetism like a large spin splitting with *d*-wave symmetry, along with a pronounced altermagnetic optical response. The presence of altermagnetic signatures necessitates a comprehensive calculation of the full magnetic exchange matrix for the rutile-structure difluoride antiferromagnet. Bilinear interactions between any two spins in a crystal can be expressed as

$$\hat{J}_{mn} = \begin{pmatrix} J_{xx} & J_{xy} & J_{xz} \\ J_{yx} & J_{yy} & J_{yz} \\ J_{zx} & J_{zy} & J_{zz} \end{pmatrix}; \quad \hat{K}_{mm} = \begin{pmatrix} K_{xx} & K_{xy} & K_{xz} \\ K_{yx} & K_{yy} & K_{yz} \\ K_{zx} & K_{zy} & k_{zz} \end{pmatrix}, \tag{1}$$

where the exchange matrix $\hat{J}_{mn}$ corresponds to the case where the two spin labels m, n reside on different crystal sites, and the single-site anisotropy matrix $\hat{K}_{mm}$ characterizes the directional dependence of the spin located at m. In the nonrelativistic limit, both matrices are rotationally invariant, that is, $\hat{J}$ is diagonal in the spin space, and $\hat{K}_{mm}$ is identically zero. Spin-orbit coupling (SOC) breaks spin-rotational symmetry and aligns spins along preferred directions which is decided by the crystal symmetry. This phenomenon introduces magnetic anisotropy, which gives rise to various noncollinear magnetic behaviors such as Kitaev interactions, spin canting, weak ferromagnetism in antiferromagnetic material, exotic topological magnetic textures, unusual magnetoelastic coupling, complex magnetic hysteresis, and many more [12–14]. If SOC can be treated perturbatively (which is the case for most 3*d* and 4*d* systems), one can show that the diagonal interactions in the $\hat{J}$ matrix appear in zero order in SOC, the antisymmetric part of the same matrix (when allowed by symmetry) in the first order, and the symmetric off-diagonal part, as well as the $\hat{K}$ matrix, in the second order. That is to say, at different levels of approximation, one can consider either purely Heisenberg exchange without any anisotropy, or Heisenberg+DMI, or the full $\hat{J}$ and $\hat{K}$ matrices. The commonly used approximation that includes $\hat{K}$ but not symmetric off-diagonal elements of $\hat{J}$ is thus inconsistent and cannot be recommended [15–19]. These considerations motivated us to explore of the full magnetic exchange matrix beyond the conventional isotropic Heisenberg and Dzyaloshinskii-Moriya interaction (DMI).

A rutilelike structure of transition metal difluorides presents a compelling platform for exploring magnetic anisotropy due to its inherent tetragonal crystal symmetry and metal-fluoride octahedral coordination. The anisotropic magnetic behavior primarily stems from the interactions among the *d* electrons of the transition metal, which are strongly influenced by the surrounding octahedral environment in the presence of SOC. This environment can be systematically tuned through variations in the choice of transition metal, metal-fluorine bond lengths, lattice parameters, and related structural parameters. The anisotropic aspects of rutile magnetism are particularly intriguing, as this system stands out as a promising candidate for investigating altermagnetism and a

[*]Contact author: ssadhukh@gmu.edu

broader landscape of correlated magnetic phenomena. In this 3*d* difluoride series, the spin orientation along [001] is favored in MnF_2, FeF_2, and CoF_2, whereas NiF_2 prefers the [011] direction [20].

Moriya [21], through an analysis of a relativistic spin Hamiltonian incorporating SOC, demonstrated that DMI cannot induce spin canting in NiF_2, but magnetic anisotropy can. However, lacking a first-principles calculation, it is nearly impossible to distinguish between the single-site anisotropy and, for instance, an Ising component of exchange coupling. Thus, Moriya in his calculation combined all anisotropic interactions in a single element of the $\hat{K}$ matrix. While Moriya's framework successfully accounts for the observed magnetic properties, a comprehensive determination of the anisotropic magnetic exchange interactions remained unaddressed. Motivated by this pioneering work, we have evaluated the complete magnetic exchange matrices for the most important bond (second nearest neighbor) connecting the corner and the central metal for four 3*d* difluorides by combining crystal symmetry analysis with first-principles density functional theory (DFT) calculations. In terms of length, this bond is the second shortest one and by far the strongest since it involves a one-stage superexchange. It is also generally considered the most important, as it allows for DMI and is responsible for the spin canting discussed by Moriya. The shortest metal-metal bond is vertical, which does not allow for DMI, and the exchange for this pair is provided by a direct metal-metal overlap and is necessarily weaker. Other exchange paths, as discussed later in the paper, are dramatically weaker. Our findings reveal the presence of ferromagnetic and antiferromagnetic elements within the exchange matrix [14,21]. Additionally, it has been reported that a finite thermal Hall conductivity can arise from intrinsic magnonic Berry curvature in altermagnetic materials with a rutile crystal structure [6–9]. Such spontaneous thermal Hall effect has been theoretically predicted for MnF_2, CoF_2, and NiF_2, which further motivated our choice of these compounds for investigating the entire magnetic exchange matrix [9]. Furthermore, optical pumping has been shown to induce significant spin canting in the insulating rutile CoF_2, with SOC playing a central role in light-induced anisotropic magnetism in altermagnets [10]. Experimental studies using x-ray magnetic dichroism have also revealed that SOC plays a dual role in the NiF_2 series, contributing not only to the anomalous Hall effect and magneto-optical conductivity but also to the emergence of weak ferromagnetism [11]. The confluence of these phenomena highlights the relevance and importance of finding an easy way to calculate the full magnetic exchange matrix. In the present work, we propose a computational approach that is both more accurate and less computationally intensive for determining all second-nearest-neighbor magnetic exchange parameters in transition metal fluorides mF_2 (where m = Mn, Fe, Co, and Ni), which crystallize in the rutile structure. Our methodology exploits the inherent symmetry of the rutile lattice to derive the minimal form of the magnetic anisotropy matrix and to formulate analytical expressions that exhibit a trigonometric dependence of the anisotropic magnetic exchange parameters on the rotation angle of the spin-quantization axis as we did earlier for kagome metal [22]. By combining these theoretically derived expressions with first-principles calculations, we achieve improved accuracy in evaluating the anisotropic exchange parameters discussed in this study.

II. CALCULATION METHODOLOGY

First-principles DFT calculations were carried out for iron group transition metal difluorides mF_2 (m = Mn, Fe, Co, and Ni) in the relativistic domain. The computations employed a plane-wave basis set with an energy cutoff of 600 eV, using projector augmented-wave pseudopotentials as implemented in VASP [23,24]. Exchange-correlation effects were treated within the generalized gradient approximation using the Perdew-Burke-Ernzerhof functional [25]. For the transition metal elements, the pseudopotentials *m_pv* (m = Mn, Fe, Co, Ni) were used, including p as valence state, along with fluorine as the ligand. Structural optimization was performed by relaxing internal atomic coordinates until the Hellmann-Feynman forces on all atoms were less than 0.001 eV/Å, and the electronic self-consistency criterion was set to 10^{-7} eV. To ensure numerical accuracy, convergence tests were conducted with k-point meshes up to $12 \times 12 \times 12$, and the resulting variations were used to assess the computational uncertainty. Additionally, a directional constraint was applied (as implemented in VASP) to ensure that only the spin-quantization axis rotates—an essential step to guarantee a simple trigonometric dependence of total energy with respect to rotation angle, in both the unit cell and the supercell setup for four transition metal difluorides.

III. CRYSTAL STRUCTURE AND SYMMETRY

The unit cell of transition metal difluorides crystallizes in the rutile structure, characterized by a tetragonal symmetry with space group $P4_2/mnm$ (SG No. 136), as shown in Figs. 1(a) and 1(b). The Wyckoff position of the transition metal is marked by ±, and the bond direction is indicated by arrows in Fig. 1(a). In Fig. 1(b), the octahedral coordination environment is illustrated, where the metal ions coordinated by fluoride ligands form edge-sharing octahedra. The lattice parameters for mF_2 (where m = Mn, Fe, Co, and Ni) have been adopted from experimentally reported data [26]. We have also indicated the local coordinate system of the octahedron by blue dotted axes and the global coordinate system by solid blue axes outside octahedral, as shown in Fig. 1(c). The $\sqrt{2} \times \sqrt{2} \times 1$ supercell of the rutile altermagnet is illustrated in Fig. 1(d), containing four nonequivalent transition metal sites. The tetragonal crystal structure exhibits several distinct symmetries. By applying the corresponding symmetry operations, we have determined the explicit form of the magnetic exchange matrix. The key symmetry operations include a fourfold screw axis (4_2) along the z direction and a mirror plane perpendicular to it. Additionally, there exists a twofold screw axis (2_1) along the x or y direction, accompanied by an n-glide plane perpendicular to it, with a mirror operation involving a fractional translation of $(\frac{1}{2}, \frac{1}{2}, 0)$. Furthermore, the structure features a twofold rotation axis along the [110] or $[1\bar{1}0]$ direction, along with a mirror plane perpendicular to these axes.

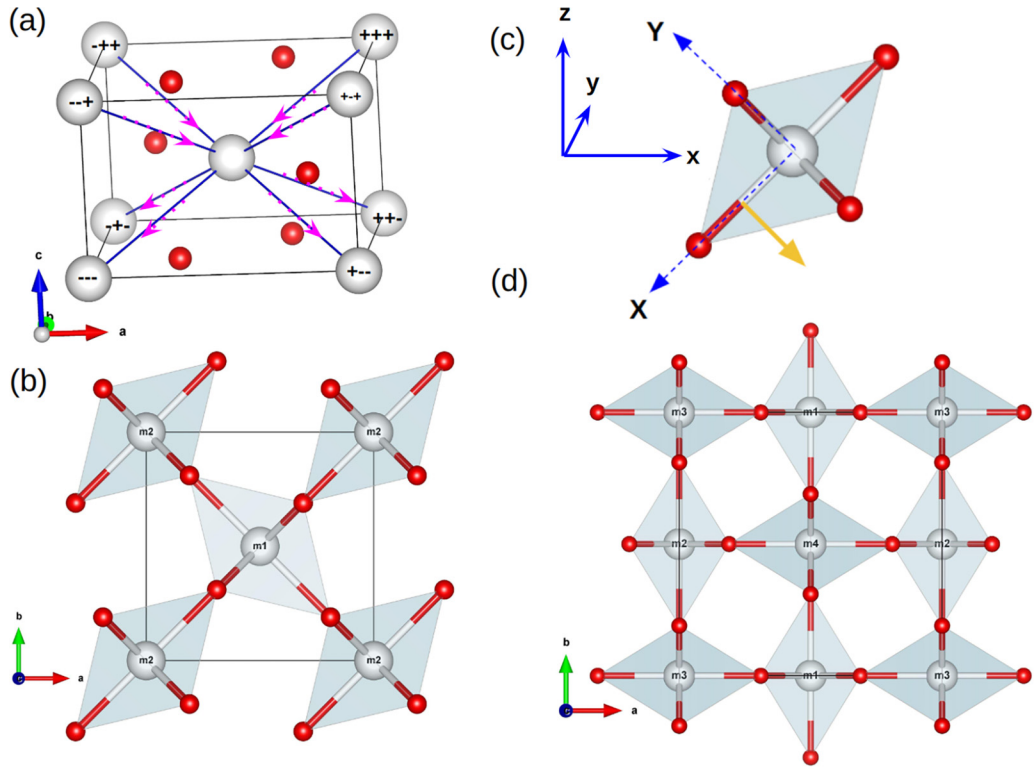

FIG. 1. (a) and (b) depict the unit cell without and with an octahedral of mF_2 (m = Mn, Fe, Co, and Ni), respectively. In these illustrations, the white spheres represent the transition metal ions m, while the red spheres denote fluorine atoms. The Wyckoff position has been marked in (a) for each transition metal atom by the combination of three ± signs. A magenta arrow also shows the bond direction. Two inequivalent magnetic sites m_1 and m_2 are labeled. (c) shows the local coordinate system of the octahedron indicated by a dotted blue arrow inside it, along the long (X) and short (Y) axes of the octahedron (uppercase X-Y), while the global coordinate system is shown outside the octahedron using solid blue lines (lowercase x-y). In contrast, the direction of the Dzyaloshinskii-Moriya (DM) vector is shown by the solid orange arrow. (d) represents the $\sqrt{2} \times \sqrt{2} \times 1$ supercell with four distinct magnetic sites—m_1, m_2, m_3, and m_4—indicated accordingly.

IV. DISCUSSION

A. Derivation of the magnetic Hamiltonian and the effect of the quantization axis rotation

The bilinear magnetic interaction in its most general form, accounting for SOC, can be expressed as discussed above

$$H = -\sum_{m,n} \mathbf{s}_m \cdot \hat{J}_{mn} \cdot \mathbf{s}_n + \sum_i \mathbf{s}_m \cdot \hat{K}_{mm} \cdot \mathbf{s}_m, \tag{2}$$

where summation is over all sites m. Here, $\hat{J}_{mn}$ and $\hat{K}_{mm}$ represent the exchange matrix and single-site anisotropy matrix as described in Eq. (1). In this case, we consider the transition metal atom to be positioned at the origin $(0, 0, 0)$. There are four second-nearest-neighbor bonds formed with other metal atoms located at positions $(\pm\frac{1}{2}, \pm\frac{1}{2}, \pm\frac{1}{2})$. The magnetic exchange interaction between the central atom and each neighboring metal atom is described by a 3×3 matrix $\hat{J}^{ijk}_{mn}$, where $i, j, k = \pm$ depends on the position of metal atoms. The system has an inversion symmetry operation that can connect eight different positions defined by i, j, and k. The crystallographic symmetry operations act differently on axial vectors (magnetic moments) than on polar vectors (dipole moments): a mirror (or glide) with normal vector $\mathbf{n}$ acting on an axial vector $\mathbf{s} = \{x, y, z\}$ transforms it as $\mathbf{s} \to 2\mathbf{n}(\mathbf{n}\cdot\mathbf{s}) - \mathbf{s}$, while the rotations about $\mathbf{n}$ act in the same way on either axial or polar vectors; for a mirror plane through (110) with $\mathbf{n} = [1\bar{1}0]$, one obtains $\mathbf{s} \to \{-y, -x, -z\}$ and all other transformation of coordinates due to symmetry operations discussed later. Now the presence of 110 mirrors through origin transforms $\mathbf{s} = \{x, y, z\}$ to $\{-y, -x, -z\}$ that leaves $J_{xy} = J_{yx} = A$, $J_{xz} = J_{yz} = B$ and $J_{zx} = J_{zy} = C$, $J_{xx} = J_{yy} = J$,

$$\begin{pmatrix} J^{+++}_{xx} & J^{+++}_{xy} & J^{+++}_{xz} \\ J^{+++}_{yx} & J^{+++}_{yy} & J^{+++}_{yz} \\ J^{+++}_{zx} & J^{+++}_{zy} & J^{+++}_{zz} \end{pmatrix} = \begin{pmatrix} J & A & B \\ A & J & B \\ C & C & J_{zz} \end{pmatrix}. \tag{3}$$

The inversion symmetry allows us to write

$$\hat{J}^{+++}_{mn} = \hat{J}^{---}_{mn} = \begin{pmatrix} J & A & B \\ A & J & B \\ C & C & J_{zz} \end{pmatrix}. \tag{4}$$

We can also write separately isotropic (J_H) and anisotropic interactions (J_z, A, B, C) like

$$J^{+++}_{mn} = J^{---}_{mn} = J_H \delta_{mn} + \begin{pmatrix} -\frac{J_z}{2} & A & B \\ A & -\frac{J_z}{2} & B \\ C & C & J_z \end{pmatrix}. \tag{5}$$

Here, J_H and J_z represent Heisenberg and Ising interactions, respectively. There is also a z mirror through the origin. It transforms $\mathbf{s} = \{x, y, z\}$ to $\{-x, -y, z\}$, leading to

$J_{xy} = J_{yx} = A$, $J_{xz} = J_{yz} = -B$ and $J_{zx} = J_{zy} = -C$, $J_{xx} = J_{yy} = J = J_H - J_z/2$. Since $B \neq C$, we can then write

$$\hat{J}^{--+}_{mn} = \hat{J}^{++-}_{mn} = J_H\delta_{mn} + \begin{pmatrix} -\frac{J_z}{2} & A & -B \\ A & -\frac{J_z}{2} & -B \\ -C & -C & J_z \end{pmatrix}. \quad (6)$$

There are also nonsymmorphic symmetry operations, i.e., a glide 100 plane at $0.25a$ from the origin, which changes $\mathbf{s} = \{x, y, z\}$ to $\{x, -y, -z\}$, and it swaps $\mathbf{s}$ and $\mathbf{s}'$, leading to

$$\hat{J}^{+--}_{mn} = \hat{J}^{-++}_{mn} = J_H\delta_{mn} + \begin{pmatrix} -\frac{J_z}{2} & -A & -C \\ -A & -\frac{J_z}{2} & C \\ -B & B & J_z \end{pmatrix}. \quad (7)$$

We have another glide plane, 010, at $0.25b$, which also swaps $\mathbf{s}$ and $\mathbf{s}'$, and it changes $\mathbf{s} = \{x, y, z\}$ to $\{-x, y, -z\}$,

$$\hat{J}^{-+-}_{mn} = \hat{J}^{+-+}_{mn} = J_H\delta_{mn} + \begin{pmatrix} -\frac{J_z}{2} & -A & C \\ -A & -\frac{J_z}{2} & -C \\ B & -B & J_z \end{pmatrix}, \quad (8)$$

so we have the total magnetic exchange matrix with the sum of (for two spins)

$$H = -\mathbf{s}_1 \cdot \sum J^{ijk}_{mn} \cdot \mathbf{s}_2, \quad (9)$$

where $J^{ijk}_{mn} = 2J^{+++}_{mn} + 2J^{--+}_{mn} + 2J^{+--}_{mn} + 2J^{-+-}_{mn}$,

$$\sum J^{ijk}_{mn} = 8J_H\delta_{mn} + \begin{pmatrix} -\frac{8J_z}{2} & 0 & 0 \\ 0 & -\frac{8J_z}{2} & 0 \\ 0 & 0 & 8J_z \end{pmatrix},$$

or we can also write it as before $J = J_H - J_z/2$ and $J_{zz} = J_H + J_z$,

$$\sum J^{ijk}_{mn} = 8\begin{pmatrix} J & 0 & 0 \\ 0 & J & 0 \\ 0 & 0 & J_{zz} \end{pmatrix}. \quad (10)$$

At this point, it is instructive to introduce a local frame, where the X axis is pointing along the longer axis of the F_6 octahedron and the Y axis along the short one. For m_1 in Fig. 1(a), the new frame is obtained by the $-\pi/4$ rotation, and for m_2, by the $+\pi/4$ rotation, or explicitly, for site 1, $X_1 = \frac{x_1+y_1}{\sqrt{2}}$, $Y_1 = \frac{y_1-x_1}{\sqrt{2}}$, and $Z_1 = z_1$, and for site 2, $X_2 = \frac{x_2-y_2}{\sqrt{2}}$, $Y_2 = \frac{x_2+y_2}{\sqrt{2}}$, and $Z_2 = z_2$. A point to be noted here is that, throughout the manuscript, the global coordinate system is denoted by the lowercase spin vectors $\mathbf{s}_1(x_1, y_1, z_1)$ and $\mathbf{s}_2(x_2, y_2, z_2)$, while the local coordinate system is represented by the uppercase spin vectors $\mathbf{S}_1(X_1, Y_1, Z_1)$ and $\mathbf{S}_2(X_2, Y_2, Z_2)$.

In the local frame, the exchange matrix appears to be

$$\hat{J}^{+++}_{mn} = J_H\delta_{mn} + \begin{pmatrix} J_x & 0 & b \\ 0 & J_y & 0 \\ c & 0 & J_z \end{pmatrix}, \quad (11)$$

where $J_x = A - J_z/2$, $J_y = A - J_z/2$, $b = \sqrt{2}B$, and $c = \sqrt{2}C$. It is clear from this representation that the diagonal exchange interaction reflects the difference between the long-long axis spin interaction and the short-short, while the long-short spins are orthogonal and do not interact, and in addition, there is symmetric compass interaction $(b + c)/2$ and a single Dzyaloshinskii-Moriya (DM) component $-(b - c)/2$ directed, in agreement with the standard rules [14,21], perpendicular to the mirror plane passing through a bond. Here, we have also added the single-site anisotropy along the long-axis anisotropy as K_l and the short-axis anisotropy as K_s of the octahedral. Hence, the total anisotropy is

$$\mathcal{H}_{\text{single-site}} = K_l\left(X_1^2 + X_2^2\right) + K_s\left(Y_1^2 + Y_2^2\right). \quad (12)$$

Considering the transformation from the local coordinate system to the global one, where $S_1 \rightarrow s_1$ and $S_2 \rightarrow s_2$, the expression of the single-site anisotropy can be written as

$$\mathcal{H}_{\text{single-site}} = 2K_-(x_1y_1 - x_2y_2) - K_+\left(z_1^2 + z_2^2\right), \quad (13)$$

where

$$K_+ = \frac{K_l + K_s}{2}, \quad K_- = \frac{K_l - K_s}{2}.$$

If we keep the spin directions of $\mathbf{s}_1$ and $\mathbf{s}_2$ fixed along the y and z axes in the global coordinate system and apply a rigid rotation of angle ϕ, the spin-quantization axis around the z axis, the resulting energy expression takes the form in the global coordinate system

$$E = E_0 - K_- \sin(2\phi). \quad (14)$$

Alternatively, if we apply a rigid rotation of the spin-quantization axis around the y axis (while keeping the spin directions of $\mathbf{s}_1$ and $\mathbf{s}_2$ along the y and z axes in the global frame), the resulting energy expression becomes in the global coordinate system

$$E = E_0 - K_+ \cos^2(\phi). \quad (15)$$

From this unit cell configuration, we can extract only the single-site anisotropies K_+ and K_- using first-principles DFT calculations. The other terms, such as A, B, C, and J_z, do not contribute by symmetry and thus fall out of the resulting energy expression. To capture additional interactions, we consider a supercell of size $\sqrt{2} \times \sqrt{2} \times 1$, which contains four spin sites, labeled $\mathbf{s}_1$, $\mathbf{s}_2$, $\mathbf{s}_3$, and $\mathbf{s}_4$ for m_1, m_2, m_3, and m_4 $3d$ transition atoms, as shown in Fig. 1(d). Transitioning to the supercell approach allows these terms to be captured and resolved through appropriate spin configurations. The Hamiltonian in supercell configuration for the four-spin site is given by

$$H = -\sum_{\substack{m=1 \\ m\neq n}}^{4}\sum_{n=1}^{4} \mathbf{s}_m \cdot J^{ijk}_{mn} \cdot \mathbf{s}_n + \mathcal{H}_{\text{single-site}}. \quad (16)$$

In the global coordinate system, by setting the spins $\mathbf{s}_1, \mathbf{s}_2, \mathbf{s}_3, \mathbf{s}_4$ along $+\hat{y}$, $-\hat{y}$, $+\hat{x}$, $-\hat{x}$, respectively, and performing a rigid rotation about the y axis, the total energy takes the

form

$$E = E_0 + [K_+ + 2(J_{zz} - J)]\cos(2\phi)$$
$$= E_0 + [K_+ + 3J_z]\cos(2\phi), \quad (17)$$

from which the Ising term J_z can be extracted. Similarly, by aligning the spins $\mathbf{s}_1, \mathbf{s}_2, \mathbf{s}_3, \mathbf{s}_4$ along $+\hat{y}, -\hat{x}, -\hat{y}, -\hat{x}$, respectively, and performing a rigid rotation about the z axis, the total energy becomes in the global coordinate system

$$E = E_0 + 16A\cos(2\phi), \quad (18)$$

which enables the extraction of the parameter A. Lastly, by setting the spin directions $\mathbf{s}_1, \mathbf{s}_2, \mathbf{s}_3, \mathbf{s}_4$ along $+\hat{x}, +\hat{y}, +\hat{z}, +\hat{x}$, respectively, and applying a rigid rotation about the z axis, the energy expression becomes in the global coordinate system

$$E = E_0 - K_- \sin(2\phi) - 4B\sin\phi - 4C\cos\phi, \quad (19)$$

which allows for the determination of the parameters B and C. We combined first-principles calculations with the analytically derived expressions presented above from the spin Hamiltonian and applied them to both unit-cell and supercell configurations. This approach enabled us to determine the symmetry-allowed minimal form of the complete magnetic exchange matrix for four distinct bonds in the iron difluoride series. A point to be noted following Moriya is that the term *nearest neighbor* is used to denote the interaction shown in Fig. 1(a), which would be the nearest-neighbor one in the ideal body-centered cubic (bcc) lattice. However, due to the strong tetrahedral distortion present in these materials, the corresponding bond is no longer a vertical metal-metal bond which is shorter. The reader needs to keep in mind that, in some papers, the nomenclature is called the *second-nearest-neighbor interaction*. This exchange interaction is by far the most dominant, and we focus on it in our calculations. For completeness, we briefly discuss the remaining exchange interactions. To this end, we employed the OpenMX code [27,28], which implements the Green's function perturbation theory based on the magnetic force theorem, and evaluated the first four isotropic exchange constants. The one we consider in the paper is J_2. The calculated ratios J_1/J_2, J_3/J_2, and J_4/J_2 for four rutile fluorides are shown Table II, and we found that J_1 is considerably smaller than J_2, and the remaining ratios are negligible. This is expected since J_2 corresponds to the shortest superexchange path and is the only such interaction mediated by a single ligand. The J_1 interaction, arising from direct metal-metal overlap, is approximately a factor of two smaller and is not expected to induce any significant effects. The detailed methodology and corresponding results are presented in the following section.

B. First-principles calculation of the exchange matrix

We have combined the equations of our theoretical model with first-principles calculations, including SOC, to evaluate the entire magnetic exchange matrix elements that contribute to the weak ferromagnetism observed in the antiferromagnetic transition metal fluorides $m\mathrm{F}_2$ (m = Mn, Fe, Co, and Ni). To the best of our knowledge, while the isotropic Heisenberg exchange interaction has been previously reported [29], the anisotropic component of the magnetic exchange interaction has not yet been explored in the literature. Leveraging the underlying symmetry of this transition metal fluoride $m\mathrm{F}_2$ series, we identify the minimal set of independent magnetic exchange parameters required to fully describe the anisotropic exchange matrix. In our computational workflow, the total energy is calculated for each rotation angle using the fixed spin configurations predicted by our model equations. To ensure systematic behavior and minimize numerical noise in our first-principles calculations, we maintain all computational parameters fixed across each dataset of one particular calculation (for a fixed spin configuration). The calculated energy difference plotted as a function of rotation angle is then fitted to the analytical expression derived from our model. As shown in Figs. S1–S5 in the Supplemental Material [30], the excellent agreement between the fitted equations with computed energy differences, especially at low energy scales, shows the accuracy and reliability of the extracted anisotropic exchange parameters. In Figs. S1–S5 in the Supplemental Material [30], the energy differences plotted along the y axis primarily represent the variation in total energy relative to the reference energy at zero rotation angle. Specifically, these differences correspond to the energy values at successive rotation angles of spin-quantization axis (e.g., 20°, 40°, and so on, up to 180°) subtracted from the energy at 0°. Our proposed method enables the extraction of anisotropic magnetic exchange interactions, namely, compass and DMIs, along with single-site anisotropy, as discussed below for the four altermagnetic rutiles: MnF_2, FeF_2, CoF_2, and NiF_2. In our approach, we use consecutive small-angle rotations of the spin-quantization axis rather than conventional total-energy mapping. This offers several advantages. First, by fixing the magnetic configuration and making only small changes in the spin-quantization axis, the systematic numerical errors due to changes in charge density, the rate of convergence, or metastability effects are avoided. Second, through small-angle rotation, the energy changes are guaranteed to remain in the linear/quadratic regime, which is crucial for determining magnetic anisotropy and exchange interactions on a small energy scale. Third, using configurations that have the two moments perpendicular to each other automatically excludes the dominating isotropic interaction J_H, also improving accuracy. Ultimately, the excellent agreement between our analytical expressions and the first-principles calculations, as shown in the trigonometric fitting curves in the Supplemental Material [30], serves as an internal consistency check that is not possible by direct energy mapping methods.

1. Magnetic exchange interactions for MnF_2

Considering the first case of MnF_2, the isotropic Heisenberg interaction is found to be -0.48 meV, as calculated from the energy difference between the ferromagnetic and antiferromagnetic configurations in the absence of SOC. Upon turning on SOC, the anisotropic magnetic exchange parameters, namely, K_+, K_-, A, B, C, and J_z, become relevant. We employed the unit cell configuration to determine the single-site anisotropies, obtaining $K_+ = -0.003$ meV and $K_- = 0.01$ meV, using Eqs. (14) and (15). The trigonometric fitting curve of the DFT data to the theoretical model is illustrated in Figs. S1(a) and S2(a) in the Supplemental Material [30]. The Ising exchange term ($J - J_{zz}$) is extracted from Eq. (17),

as shown in Fig. S3(a) in the Supplemental Material [30], and used to evaluate J_z via the relation $-\frac{3}{2}J_z = J - J_{zz}$. The anisotropic exchange parameters A, B, and C are calculated using Eqs. (18) and (19) from the supercell configurations. The quality of the fitting procedure for determining these parameters is demonstrated in Figs. S4(a) and S5(a) in the Supplemental Material [30]. To ensure the robustness of the extracted anisotropy values, we have tested convergence by employing two different k-meshes: $6 \times 6 \times 6$ and $8 \times 8 \times 8$, in both in-plane and out-of-plane directions for all cases. Hence, the complete magnetic exchange interaction for MnF_2 is given by following Eq. (5) as

$$J_{mn}^{+++} = -0.48\delta_{mn} + \begin{pmatrix} 0 & 0 & -0.01 \\ 0 & 0 & -0.01 \\ -0.01 & -0.01 & 0 \end{pmatrix}, \quad (20)$$

where the first term represents the isotropic Heisenberg interaction, and the matrix captures the anisotropic contributions induced by SOC. Following a similar procedure, we can express the matrix forms of the exchange interactions $\hat{J}_{mn}^{--+}$, $\hat{J}_{mn}^{+--}$, and $\hat{J}_{mn}^{-+-}$ as given in Eqs. (6)–(8), respectively. The fact that the Mn^{2+} ion has a closed $3d$ shell explains why spin-orbit interaction, and thus anisotropic exchange, is so small. The anisotropic contribution can also be expressed in the local coordinate system of the octahedron, which provides a more convenient framework for describing magnetic exchange interactions. This is achieved by performing a coordinate transformation, leading to Eq. (11). Hence, J_{mn}^{+++} is now in the local coordinate system

$$J_{mn}^{+++} = -0.48\delta_{mn} + \begin{pmatrix} 0 & 0 & -0.02 \\ 0 & 0 & 0 \\ -0.02 & 0 & 0 \end{pmatrix}.$$

From the above exchange matrix, we can see that symmetric compass interactions are around -0.02 meV, while the anisotropic DMI is zero. Hence, the total Hamiltonian for the exchange interaction in a local coordinate system with two spins $S_1(X_1, Y_1, Z_1)$ and $S_2(X_2, Y_2, Z_2)$ can be written as

$$\begin{aligned} H_{MnF_2} &= 0.48\,(\mathbf{S}_1 \cdot \mathbf{S}_2) + 0.02(X_1Z_2 + Z_1X_2) \\ &\quad + 0.007\left(X_1^2 + X_2^2\right) + 0.013\left(Y_1^2 + Y_2^2\right). \end{aligned} \quad (21)$$

The above equation provides a complete description of magnetic exchange interactions for MnF_2, with $K_l(K_+ + K_-)$ and $K_s(K_+ - K_-)$, as long- and short-axis anisotropies are 0.007 and 0.013 meV.

2. Magnetic exchange interactions for FeF_2

For the second compound FeF_2, the isotropic Heisenberg interaction J_H is found to be -0.66 meV. The single-site anisotropies were obtained as $K_+ = 0.46$ meV and $K_- = 0.55$ meV using Eqs. (14) and (15). The trigonometric fitting of the DFT data to the theoretical model is shown in Figs. S1(b) and S2(b) in the Supplemental Material [30]. The Ising exchange related term $(J - J_{zz})$ was extracted from Eq. (17) (Fig. S3(b) in the Supplemental Material [30]) . The anisotropic exchange parameters A, B, and C are evaluated from Eqs. (18) and (19), with the fitting results illustrated in Figs. S4(b) and S5(b) in the Supplemental Material [30]. The complete magnetic exchange interaction for FeF_2 is given by using Eq. (5),

$$J_{mn}^{+++} = -0.66\delta_{mn} + \begin{pmatrix} -0.07 & 0 & 0.06 \\ 0 & -0.07 & 0.06 \\ 0.02 & 0.02 & 0.15 \end{pmatrix}, \quad (22)$$

where the first term denotes the isotropic interaction, and the matrix encodes the SOC-induced anisotropic contributions. Following a similar approach, the exchange matrices $\hat{J}_{mn}^{--+}$, $\hat{J}_{mn}^{+--}$, and $\hat{J}_{mn}^{-+-}$ are given in Eqs. (6)–(8). The anisotropic part can also be expressed in the local coordinate system of the octahedron as given in Eq. (11),

$$J_{mn}^{+++} = -0.66\delta_{mn} + \begin{pmatrix} -0.07 & 0 & 0.08 \\ 0 & -0.07 & 0 \\ 0.03 & 0 & 0.15 \end{pmatrix}.$$

Here, the symmetric compass interactions are around 0.06 meV, while the anisotropic DMI is approximately -0.03 meV. Hence, the total Hamiltonian for the exchange interaction can be written as considering the single-site anisotropies K_l and K_s,

$$\begin{aligned} H_{FeF_2} &= 0.66\,(\mathbf{S}_1 \cdot \mathbf{S}_2) + 0.07\,(X_1X_2 + Y_1Y_2) - 0.15\,Z_1Z_2 \\ &\quad - 0.06(X_1Z_2 + Z_1X_2) + 0.03(Z_1X_2 - X_1Z_2) \\ &\quad + 1.01\left(X_1^2 + X_2^2\right) + 0.09\left(Y_1^2 + Y_2^2\right). \end{aligned} \quad (23)$$

The above equation provides a complete description of the magnetic exchange interactions in FeF_2.

3. Magnetic exchange interactions for CoF_2

For CoF_2, the isotropic Heisenberg interaction is $J_H = -1.01$ meV. The single-site anisotropy parameters, extracted using Eqs. (14) and (15), are $K_+ = 0.96$ meV and $K_- = 0.85$ meV. The trigonometric fit of DFT data to the theoretical model is shown in Figs. S1(c) and S2(c) in the Supplemental Material [30], and the Ising exchange term $(J - J_{zz})$, obtained from Eq. (17), is presented in Fig. S3(c) in the Supplemental Material [30]. The fitting quality is illustrated in Figs. S4(c) and S5(c) in the Supplemental Material [30] to find A, B, and C. Thus, the full magnetic exchange interaction for CoF_2 is given by Eq. (5),

$$J_{mn}^{+++} = -1.01\delta_{mn} + \begin{pmatrix} -0.16 & 0 & 0.17 \\ 0 & -0.16 & 0.17 \\ 0.13 & 0.13 & 0.32 \end{pmatrix}. \quad (24)$$

Here, the first term denotes the isotropic Heisenberg interaction, while the matrix encapsulates anisotropic contributions arising from the relativistic domain (SOC). The corresponding exchange matrices $\hat{J}_{mn}^{--+}$, $\hat{J}_{mn}^{+--}$, and $\hat{J}_{mn}^{-+-}$ are presented in Eqs. (6)–(8), respectively. The anisotropic part in the local octahedral coordinate system [following Eq. (11)] is

$$J_{mn}^{+++} = -1.01\delta_{mn} + \begin{pmatrix} -0.16 & 0 & 0.24 \\ 0 & -0.16 & 0 \\ 0.18 & 0 & 0.32 \end{pmatrix},$$

with symmetric compass interactions $\sim$0.21 meV and anisotropic DMI ~ -0.03 meV. The total exchange Hamilto-

nian is with $K_l = 1.81$ meV and $K_s = 0.11$ meV,

$$H_{\mathrm{CoF_2}} = 1.01\,(\mathbf{S}_1 \cdot \mathbf{S}_2) + 0.16\,(X_1X_2 + Y_1Y_2) - 0.32\,Z_1Z_2 - 0.21\,(X_1Z_2 + Z_1X_2) + 0.03\,(Z_1X_2 - X_1Z_2) + 1.81\left(X_1^2 + X_2^2\right) + 0.11\left(Y_1^2 + Y_2^2\right). \quad (25)$$

4. Magnetic exchange interactions for NiF_2

The end compound of this series NiF_2 is particularly intriguing, as the spins in these materials exhibit a preference for tilting along the z axis. Here, the isotropic Heisenberg interaction is $J_H = -4.11$ meV. The single-site anisotropies, obtained from Eqs. (14) and (15), are $K_+ = -0.15$ meV and $K_- = 0.07$ meV. The Ising exchange term $(J - J_{zz})$, along with the other anisotropic parameters (A, B, C), was extracted from the trigonometric relations in the same manner as for the three other compounds in the series. The corresponding fitting curves for all parameters (K_+, K_-, J_z, A, B, C) are presented in Figs. S1(d)–S5(d) in the Supplemental Material [30]. The complete exchange interaction is given by Eq. (5),

$$J_{mn}^{+++} = -4.11\delta_{mn} + \begin{pmatrix} -0.02 & 0 & 0.31 \\ 0 & -0.02 & 0.31 \\ 0.30 & 0.30 & 0.04 \end{pmatrix}. \quad (26)$$

The first term is isotropic, while the matrix captures anisotropic terms due to SOC corrections, as discussed earlier. The matrices $\hat{J}_{mn}^{--+}$, $\hat{J}_{mn}^{+--}$, and $\hat{J}_{mn}^{-+-}$ follow from Eqs. (6)–(8). The anisotropic part in the local octahedral coordinate system [Eq. (11)] is

$$J_{mn}^{+++} = -4.11\delta_{mn} + \begin{pmatrix} -0.02 & 0 & 0.44 \\ 0 & -0.02 & 0 \\ 0.42 & 0 & 0.04 \end{pmatrix},$$

with symmetric compass interactions $\sim$0.43 meV and anisotropic DMI ~ -0.01 meV. Hence, the total exchange Hamiltonian can be written considering $K_l = 0.08$ meV and $K_s = 0.22$ meV,

$$H_{\mathrm{NiF_2}} = 4.11\,(\mathbf{S}_1 \cdot \mathbf{S}_2) + 0.02\,(X_1X_2 + Y_1Y_2) - 0.04\,Z_1Z_2 - 0.43\,(X_1Z_2 + Z_1X_2) + 0.01\,(Z_1X_2 - X_1Z_2) + 0.08\left(X_1^2 + X_2^2\right) + 0.22\left(Y_1^2 + Y_2^2\right). \quad (27)$$

5. Comparison

We have plotted the isotropic and anisotropic exchange parameters as a function of the transition metal elements from Mn to Ni, as shown in Figs. 2 and 3(a)–3(f). The variation in the isotropic exchange parameters observed in our calculations follows trends similar to those found in the available literature [29]. For the anisotropic exchange parameters, two distinct trends emerge, corresponding to the sum and the difference of the DM and the compass term. First, the trends of the Ising interaction J_z and the strength of anisotropy constants K_+ and K_- are similar, which show distinct peaks in the case of FeF_2 and CoF_2 in comparison with MnF_2 and NiF_2, as shown in Figs. 3(a)–3(c). In our rutile fluoride systems, the relativistic effects mainly arise from the SOC of d electrons, split into t_{2g} and e_g manifolds, separated by the crystal field energy $\Delta = 10Dq \sim 1$ eV—as opposed to some systems with very heavy ligands, like CrI_3, where the large SOC on the ligands may play a significant role. The anisotropic exchange parameters are mainly controlled by the SOC strength, which is strongly affected by orbital quenching. A strong orbital quenching reduces the orbital moment, making the $\mathbf{L} \cdot \mathbf{S}$ interaction weaker, while a reduced orbital quenching increases the anisotropic magnetic interactions. Here, Mn^{2+} has a complete d^5 shell with zero orbital moment, so SOC there is extremely weak, as reflected in anisotropic magnetic interactions. Also, Ni^{2+} has a complete t_{2g} shell, so the orbital moments appear only in the second order in $\xi_{\mathrm{SOC}}/\Delta$, a rather small number. On the other hand, FeF_2 and CoF_2 have one hole or one electron in the t_{2g} shell, respectively, which can form a combination with $L_z = \pm 1$, resulting in stronger SOC, thus enhancing the anisotropic magnetic constants K^+, K^-, and J_z, see Fig. 3, as well as DMI interaction $(B - C)/\sqrt{2}$, see Table II.

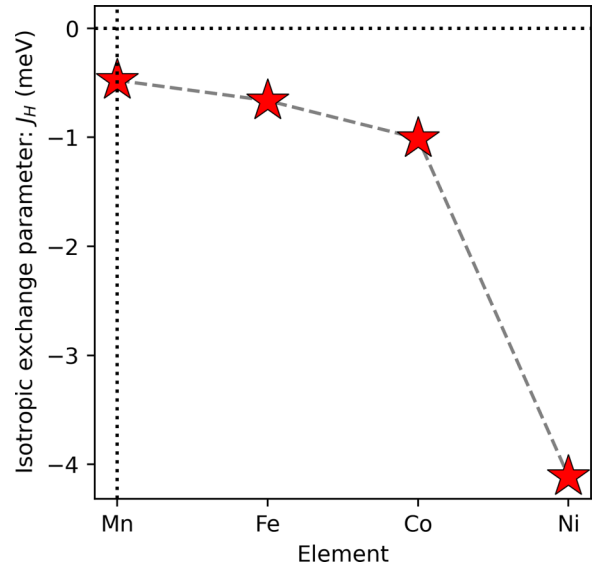

FIG. 2. Illustration of the isotropic exchange parameter (J_H) for each transition metal in the mF_2 compound, where $m =$ Mn, Fe, Co, Ni.

Surprisingly, the compass interaction $(B + C)/\sqrt{2}$ does not follow this trend but varies consistently with the Heisenberg exchange interaction J_H, with the maximum for NiF_2 and minimum for MnF_2. To understand this, we note that the Heisenberg interaction for NiF_2 is significantly higher (by at least a factor of 4) than that for the other compounds. As discussed in Ref. [29], this is due to its enhanced metal-fluorine

TABLE I. The lattice parameters a and c for the four transition metal difluorides have been presented, along with the two distinct metal-fluorine bond lengths. The lattice parameters were chosen to closely match those reported in the experimental study Ref. [26].

	Lattice parameters		Bond length (m-F)	
Elements	a(Å)	c(Å)	d_1(Å)	d_2(Å)
MnF_2	4.87	3.31	2.14	2.11
FeF_2	4.70	3.31	2.03	2.10
CoF_2	4.70	3.18	2.05	2.04
NiF_2	4.65	3.08	2.04	1.98

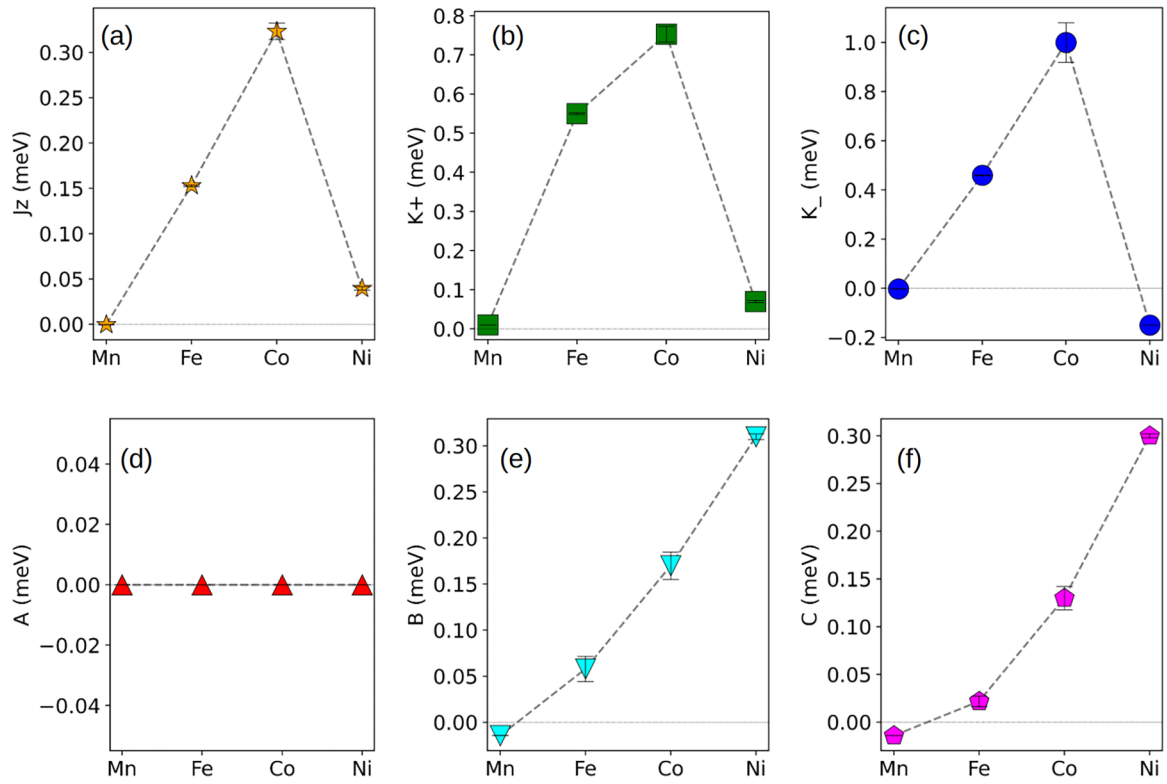

FIG. 3. (a)–(f) show the anisotropic magnetic exchange parameters (i.e., magnetic interactions in the presence of SOC) for each transition metal in the mF_2 compound, where $m =$ Mn, Fe, Co, and Ni in the global coordinate system. Specifically, (a) displays the Ising term (J_z), (b) shows the single-site anisotropy K_+, (c) presents the single-site anisotropy K_-, and (d)–(f) correspond to the parameters A, B, and C, respectively. The detailed definitions and discussions of these exchange parameters are provided in the main text. The fitting errors are indicated in each figure by the bars and are roughly on the order of the size of the marker.

hybridization. Here, NiF_2 exhibits the smallest metal-fluorine energy splitting as well as the shortest average m–F bond length across the series. These features significantly enhance the t_{pd} hopping between Ni-d and F-p orbitals, resulting in a stronger superexchange pathway. Additionally, the larger superexchange angle further enhances the AFM interaction. Coming back to the compass interaction, we observe that, while its absolute value bucks the predicted trend, its ratio to J_H is small in NiF_2, following that trend. The results of all calculations are summarized in Tables I and II. We confirm that the out-of-plane single-site anisotropy ($-K_+$) combined with the Ising term (J_z) yields the easy-axis anisotropy for all compounds except NiF_2. For the latter, we have applied Moriya's theory [21], using our calculated in-plane single-site anisotropy $2K^-$, to find the spin-canting angle for NiF_2. The spin-canting angle is 0.38°, well within the reported range [31].

TABLE II. Magnetic exchange interaction ratios for four rutile fluorides, where J_1 represents the first-nearest-neighbor interaction, J_2 the second-nearest-neighbor interaction, J_3 the third-nearest-neighbor interaction, and J_4 the fourth-nearest-neighbor interaction.

Metal fluorides	J_1/J_2	J_3/J_2	J_4/J_2
MnF_2	0.47	0.010	0.05
FeF_2	0.12	0.002	0.05
CoF_2	0.54	0.013	0.007
NiF_2	0.38	0.019	0.03

V. SUMMARY AND CONCLUSIONS

In summary, we have developed a computational framework that uses symmetry analysis to construct a theoretical model with trigonometric expressions of the rotation angle of the spin-quantization axis vs energy, which are subsequently fitted to the angular dependence of total energy obtained from first-principles calculations. This approach facilitates the extraction of anisotropic magnetic exchange interactions, a relatively underexplored domain within computational magnetism. As a case study, we apply this method to a series of magnetic transition metal fluorides (mF_2, where $m =$ Mn, Fe, Co, and Ni), chosen for their characteristic weak ferromagnetism or altermagnetism that can be effectively captured through anisotropic exchange terms, which are a mixture of ferromagnetic and antiferromagnetic contributions. Our analysis reveals that MnF_2 and NiF_2 exhibit the smallest and largest values, respectively, of both isotropic (J_H) and anisotropic exchange parameters B and C. In contrast, FeF_2 and CoF_2 display significantly larger single-site anisotropies, not only along the principal axes of the octahedral coordination but also in the Ising-like term, relative to the end-member compounds due to the orbital quenching effect. Ultimately, we have determined the compass and DMIs, as well as the

single-site anisotropy, in the local coordinate system using coordinate transformations. The proposed method is computationally efficient and robust, with minimal numerical noise, as all computational parameters are held constant except for the rotation angle of the spin-quantization axis. The high quality of the fitted equations demonstrates excellent agreement between the symmetry-derived model and first-principles data. This methodology offers a powerful and generalizable tool for determining the complete magnetic exchange matrix in a wide range of magnetic materials, thereby offering valuable insights into the origin of unusual magnetic phenomena.

ACKNOWLEDGMENTS

This work was supported by the Army Research Office under Cooperative Agreement No. W911NF-22-2-0173. We also acknowledge support from QSEC and computational resources from the Hopper HPC cluster at GMU. Crystal structure visualizations were produced with the aid of the VESTA software package [32]. We would like to thank Po-hao Chang and Bishal Thapa for the fruitful discussion.

DATA AVAILABILITY

The data that support the findings of this article are not publicly available upon publication because it is not technically feasible and/or the cost of preparing, depositing, and hosting the data would be prohibitive within the terms of this research project. The data are available from the authors upon reasonable request.

[1] P. Keßler, L. Garcia-Gassull, A. Suter, T. Prokscha, Z. Salman, D. Khalyavin, P. Manuel, F. Orlandi, I. I. Mazin, R. Valentí, *et al.*, Absence of magnetic order in RuO_2: Insights from μSR spectroscopy and neutron diffraction, npj Spintron. **2**, 50 (2024).

[2] M. Hiraishi, H. Okabe, A. Koda, R. Kadono, T. Muroi, D. Hirai, and Z. Hiroi, Nonmagnetic ground state in RuO_2 revealed by muon spin rotation, Phys. Rev. Lett. **132**, 166702 (2024).

[3] L. Kiefer, F. Wirth, A. Bertin, P. Becker, L. Bohatý, K. Schmalzl, A. Stunault, J. A. Rodríguez-Velamazan, O. Fabelo, and M. Braden, Crystal structure and absence of magnetic order in single-crystalline RuO_2, J. Phys.: Condens. Matter **37**, 135801 (2025).

[4] J. Liu, J. Zhan, T. Li, J. Liu, S. Cheng, Y. Shi, L. Deng, M. Zhang, C. Li, J. Ding, *et al.*, Absence of altermagnetic spin-splitting character in rutile oxide RuO_2, Phys. Rev. Lett. **133**, 176401 (2024).

[5] G. Yumnam, P. R. Raghuvanshi, J. D. Budai, D. Bansal, L. Bocklage, D. Abernathy, Y. Cheng, A. Said, I. I. Mazin, H. Zhou, *et al.*, Constraints on magnetism and correlations in RuO_2 from lattice dynamics and Mössbauer spectroscopy, Cell Rep. Phys. Sci. **6**, 102852 (2025).

[6] K. Takahashi, C. R. W. Steward, M. Ogata, R. M. Fernandes, and J. Schmalian, Elasto-Hall conductivity and the anomalous Hall effect in altermagnets, Phys. Rev. B **111**, 184408 (2025).

[7] C. Song, H. Bai, Z. Zhou, L. Han, H. Reichlová, J. H. Dil, J. Liu, X. Chen, and F. Pan, Altermagnets as a new class of functional materials, Nat. Rev. Mater. **10**, 473 (2025).

[8] X. Zhou, W. Feng, R.-W. Zhang, L. Šmejkal, J. Sinova, Y. Mokrousov, and Y. Yao, Crystal thermal transport in altermagnetic RuO_2, Phys. Rev. Lett. **132**, 056701 (2024).

[9] R. Hoyer, R. J. Ubiergo, K.-H. Ahn, L. Šmejkal, and A. Mook, Spontaneous crystal thermal Hall effect in insulating altermagnets, Phys. Rev. B **111**, L020412 (2025).

[10] T. Adamantopoulos, M. Merte, F. Freimuth, D. Go, L. Zhang, M. Ležaić, W. Feng, Y. Yao, J. Sinova, L. Šmejkal, *et al.*, Spin and orbital magnetism by light in rutile altermagnets, npj Spintron. **2**, 46 (2024).

[11] A. Hariki, K. Sakurai, T. Okauchi, and J. Kuneš, Separating altermagnetic and ferromagnetic effects in x-ray magnetic dichroism of rutile NiF_2, npj Quantum Mater. **10**, 49 (2025).

[12] G. Sala, J. Y. Y. Lin, A. M. Samarakoon, D. S. Parker, A. F. May, and M. B. Stone, Ferrimagnetic spin waves in honeycomb and triangular layers of $Mn_3Si_2Te_6$, Phys. Rev. B **105**, 214405 (2022).

[13] P. A. Maksimov, Z. Zhu, S. R. White, and A. L. Chernyshev, Anisotropic-exchange magnets on a triangular lattice: Spin waves, accidental degeneracies, and dual spin liquids, Phys. Rev. X **9**, 021017 (2019).

[14] T. Moriya, Anisotropic superexchange interaction and weak ferromagnetism, Phys. Rev. **120**, 91 (1960).

[15] K. M. Ranjith, S. Luther, T. Reimann, B. Schmidt, Ph. Schlender, J. Sichelschmidt, H. Yasuoka, A. M. Strydom, Y. Skourski, J. Wosnitza, *et al.*, Anisotropic field-induced ordering in the triangular-lattice quantum spin liquid $NaYbSe_2$, Phys. Rev. B **100**, 224417 (2019).

[16] H. Yang, J. Liang, and Q. Cui, First-principles calculations for Dzyaloshinskii-Moriya interaction, Nat. Rev. Phys. **5**, 466 (2023).

[17] K. Di, V. L. Zhang, H. S. Lim, S. C. Ng, M. H. Kuok, J. Yu, J. Yoon, X. Qiu, and H. Yang, Direct observation of the Dzyaloshinskii-Moriya interaction in a Pt/Co/Ni film, Phys. Rev. Lett. **114**, 047201 (2015).

[18] P. P. Stavropoulos, D. Pereira, and H.-Y. Kee, Microscopic mechanism for a higher-spin Kitaev model, Phys. Rev. Lett. **123**, 037203 (2019).

[19] H. Takagi, T. Takayama, G. Jackeli, G. Khaliullin, and S. E. Nagler, Concept and realization of Kitaev quantum spin liquids, Nat. Rev. Phys. **1**, 264 (2019).

[20] A. Palmer and W. Jauch, On the domain structure in NiF_2: A γ-ray diffraction study, Solid State Commun. **77**, 95 (1991).

[21] T. Moriya, Theory of magnetism of NiF_2, Phys. Rev. **117**, 635 (1960).

[22] S. Sadhukhan, B. Thapa, and I. I. Mazin, First-principles study of the magnetic anisotropic exchange interactions and magnetoelastic coupling in Fe-based kagome metals, Phys. Rev. B **112**, 144433 (2025).

[23] G. Kresse and J. Hafner, *Ab initio* molecular dynamics for liquid metals, Phys. Rev. B **47**, 558(R) (1993).

[24] G. Kresse and J. Furthmüller, Efficient iterative schemes for *ab initio* total-energy calculations using a plane-wave basis set, Phys. Rev. B **54**, 11169 (1996).
[25] J. P. Perdew, K. Burke, and M. Ernzerhof, Generalized gradient approximation made simple, Phys. Rev. Lett. **77**, 3865 (1996).
[26] J. W. Stout and S. A. Reed, Magnetic anisotropy of the iron-group fluorides, J. Am. Chem. Soc. **76**, 5279 (1954).
[27] T. Ozaki, Variationally optimized atomic orbitals for large-scale electronic structures, Phys. Rev. B **67**, 155108 (2003).
[28] T. Ozaki and H. Kino, Numerical atomic basis orbitals from H to Kr, Phys. Rev. B **69**, 195113 (2004).
[29] H. Das, S. Kanungo, and T. S. Dasgupta, First-principles study of magnetoelastic effect in the difluoride compounds MF_2 (M = Mn, Fe, Co, Ni), Phys. Rev. B **86**, 054422 (2012).
[30] See Supplemental Material at http://link.aps.org/supplemental/10.1103/h1ld-4gxc for the trigonometric fitting curve used to calculate the anisotropic exchange parameters for the four altermagnetic rutile fluorides.
[31] H. Shi, D. Lederman, K. V. O'Donovan, and J. A. Borchers, Exchange bias and enhancement of the Néel temperature in thin NiF_2 films, Phys. Rev. B **69**, 214416 (2004).
[32] K. Momma and F. Izumi, VESTA 3 for three-dimensional visualization of crystal, volumetric and morphology data, J. Appl. Crystallogr. **44**, 1272 (2011).